Pressure-Induced Superconductivity and Flattened Se_6 Rings in the Wide Band Gap Semiconductor $Cu_2I_2Se_6$

Weizhao Cai,[†] Wenwen Lin,[‡] Long-Hua Li,*[,§] Christos D. Malliakas,[∥] Rong Zhang,[†]
Matthew Groesbeck,[†] Jin-Ke Bao,[‡] Dongzhou Zhang,[⊥] Eran Sterer,[†,#] Mercouri G. Kanatzidis,*[,‡,∥]
and Shanti Deemyad*[,†]

[†]Department of Physics and Astronomy, University of Utah, Salt Lake City, Utah 84112, United States
[‡]Materials Science Division, Argonne National Laboratory, Argonne, Illinois 60439, United States
[§]School of Chemistry and Chemical Engineering, Jiangsu University, Zhenjiang 212013, China
[∥]Department of Chemistry, Northwestern University, Evanston, Illinois 60208, United States
[⊥]PX2, Hawaii Institute of Geophysics and Planetology, University of Hawaii at Manoa, Honolulu, Hawaii 96822, United States
[#]Department of Physics, Nuclear Research Center, Negev, P.O. Box 9001, Beer-Sheva 84190, Israel

S *Supporting Information*

ABSTRACT: The two major classes of unconventional superconductors, cuprates and Fe-based superconductors, have magnetic parent compounds, are layered, and generally feature square-lattice symmetry. We report the discovery of pressure-induced superconductivity in a nonmagnetic and wide band gap 1.95 eV semiconductor, $Cu_2I_2Se_6$, with a unique anisotropic structure composed of two types of distinct molecules: Se_6 rings and Cu_2I_2 dimers, which are linked in a three-dimensional framework. $Cu_2I_2Se_6$ exhibits a concurrent pressure-induced metallization and superconductivity at ∼21.0 GPa with critical temperature (T_c) of ∼2.8 K. The T_c monotonically increases within the range of our study reaching ∼9.0 K around 41.0 GPa. These observations coincide with unprecedented chair-to-planar conformational changes of Se_6 rings, an abrupt decrease along the

c-axis, and negative compression within the *ab* plane during the phase transition. DFT calculations demonstrate that the flattened Se_6 rings within the CuSe layer create a high density of states at the Fermi level. The unique structural features of $Cu_2I_2Se_6$ imply that superconductivity may emerge in anisotropic Cu-containing materials without square-lattice geometry and magnetic order in the parent compound.
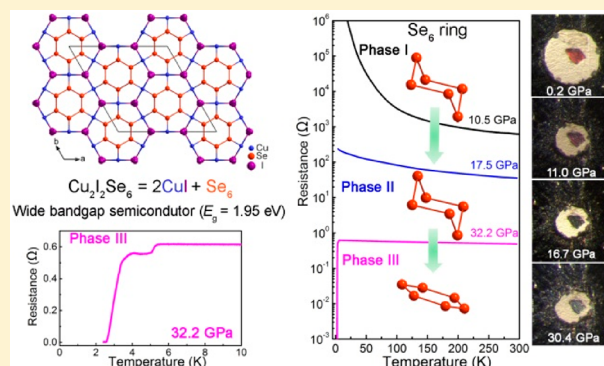
INTRODUCTION

Superconductivity in cuprates is one of the most fascinating and yet not well understood phenomena in condensed matter.[1−5] Almost all high-T_c cuprates have perovskite-type structure with the two-dimensional (2D) square CuO_2 planes acting as conduction layers, and their parent compounds are antiferromagnetic Mott insulators.[6] Magnetism and charge order in the CuO_2 plane are thought to play major roles in the superconductivity.[7,8] A decade ago, a closely related superconducting family, Fe-based compounds $LaO_{1−x}F_xFeAs$[9] and $A_xFe_{2−y}Se_2$ (A = K, Cs, Rb)[10,11] were discovered. Similar to cuprate superconductors having a CuO_2 layer, Fe-based superconductors (FeSCs) structurally feature a square-lattice of iron atoms tetrahedrally coordinated to X atoms (X = pnictide or chalcogenide) that are stacked above and below the iron lattice. The common edge-sharing FeX_4 tetrahedra are considered a crucial ingredient in stabilizing the superconductivity.[12] The phase diagram of both cuprates and

FeSCs can be modified using either chemical substitution (i.e., electron or hole doping) or external pressure, which effectively drives the antiferromagnetic (AFM) state to a superconducting state without changing the parent structure.[13] The superconducting transition temperature (T_c) of both families of compounds strongly depends on the charge transfer between the conducting and insulating layers, which can also be tuned by application of external pressure or by chemical doping.[14−16]

Superconductivity in materials with chemical and compositional similarities to cuprates and FeSCs has been a subject of intensive research for both understanding the systematics of structural and electronic changes that prompts these extraordinary superconducting states and discovery of other families of high-T_c superconductors. Although pressure-induced superconductivity has been reported in a small

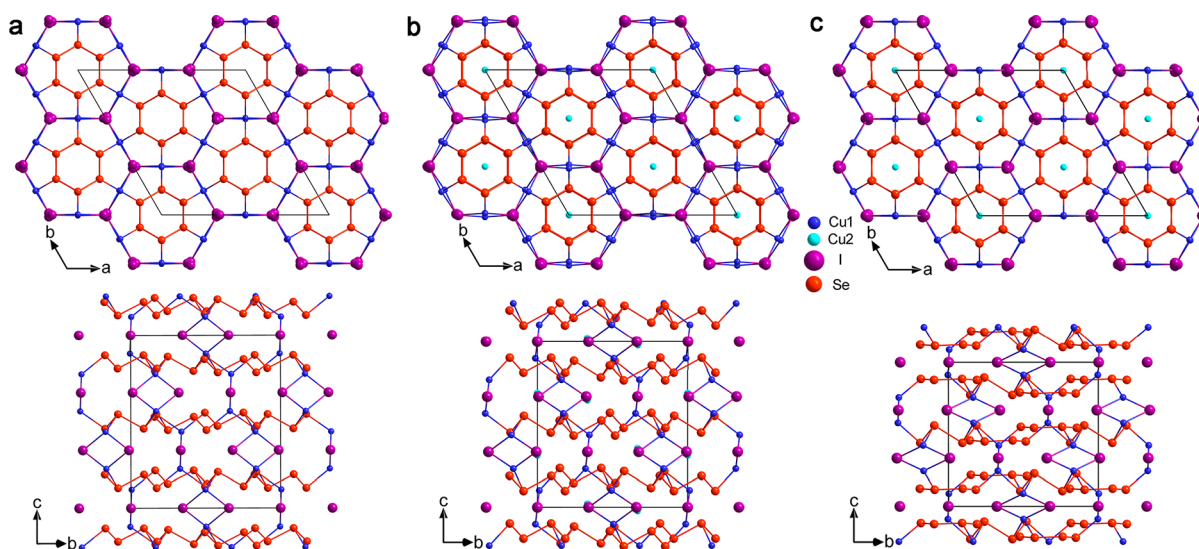**Figure 1.** Crystal structures of $Cu_2I_2Se_6$. (a) Phase I at 0.2 GPa, (b) phase II at 19.2 GPa, and (c) phase III at 35.8 GPa. Color code: blue atoms Cu1, purple I, bright red Se. The disordered Cu2 atoms at the $6c$ site in panels b and c are represented as cyan. For clarity, the shortest Cu1−Cu1′ bonds within Cu_2I_2 rhomboids are omitted.
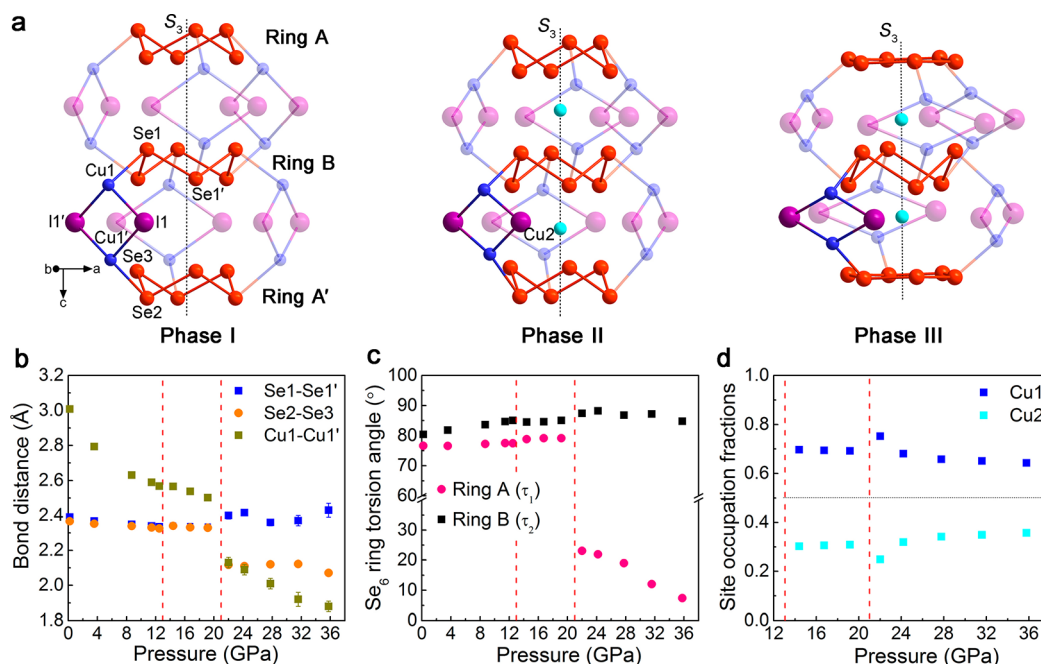

Figure 2. Evolution of structural parameters of $Cu_2I_2Se_6$ as a function of pressure. (a) The structural changes of "lantern-shaped" building blocks of $Cu_2I_2Se_6$ compressed in helium as the pressure medium. The S_3-symmetry is indicated as black dashed line. In phases II and III, the initial Wyckoff site $18h$ Cu1 atoms partially migrated to the $6c$ site (Cu2). Two different types of Se_6 rings, ring A (symmetrically equivalent to ring A′) and ring B, are indicated. For clarity, the Se atoms that are bonded to the tetrahedrally coordinated Cu1 atoms are partially omitted (cf. Figure S2a). And the newly formed Cu1−Cu1′ and Cu2−Se1 bonds are also omitted in phases II and III. (b) Compression of Se−Se and Cu1−Cu1′ bond lengths. (c) Evolution of Se−Se−Se−Se torsion angles τ_1 and τ_2 in ring A and ring B under pressure. (d) Site occupation fractions (SOFs) of the Cu1 and Cu2 atoms versus pressure.

number of magnetic FeSCs and cuprates without square-lattice geometry including one-dimensional ladder structure $BaFe_2S_3$[17] and $Sr_{0.4}Ca_{13.6}Cu_{24}O_{41.84}$[18] as well as 2D honeycomb lattice $FePSe_3$,[19] until now, superconductivity in a nonbinary copper-containing material without square lattice symmetry with an absence of magnetic order in the parent compound has not been reported. In this work, we studied the pressure dependence of the structural and electronic properties of the copper iodide triselenide ($Cu_2I_2Se_6$), which is a

nonmagnetic copper-containing wide band gap semiconductor (∼1.95 eV) lacking square lattice symmetry.[20] We find that the application of high pressure drastically modifies the electronic properties of $Cu_2I_2Se_6$, which causes a semiconductor-to-metal transition and superconductivity while maintaining the crystal symmetry of the parent structure. Superconductivity in binary Cu-chalcogenides, $CuSe_2$ and CuS, with $T_c < 2$ K at ambient pressure was reported previously.[21,22] However, to our knowledge $Cu_2I_2Se_6$ is the first observation of super-

conductivity in a nonmagnetic ternary Cu-containing material without square lattice geometry.

$Cu_2I_2Se_6$ is a coinage metal (silver and copper) halide chalcogenide in which distinct rhomboidal Cu_2I_2 dimers and cyclohexane-like Se_6 rings make up the crystal structure. This special class of semiconductors often exhibit pronounced structural disorder and high ion dynamics at elevated temperatures and undergo superionic phase transitions with the emergence of mobile ions in the substructure.[23] The structures of these superionic phases usually have lattice sites with lower energy barriers, facilitating mobility of small Ag^+/ Cu^+ ions.[24] While the temperature dependence of the properties of coinage metal halide chalcogenides has been extensively studied, their high pressure behavior has rarely been studied. $Cu_2I_2Se_6$, which is not superionic at ambient pressure, can be structurally rationalized as a composite material with neutral Se_6 molecules (ligands) and Cu_2I_2 molecular dimers linked to form a 3D framework.[25] The structure is truly a molecular assembly of Se_6 rings and rhombic Cu_2I_2 molecules as the removal of one type of molecule (e.g., Se_6 or Cu_2I_2) from the structure leaves isolated molecules of the other type rather than a continuous infinite substructure. The compound is valence-precise and also a semiconductor with a wide band gap of 1.95 eV and high room temperature electrical resistivity of $\sim 10^{12}$ Ω·cm.[20] $Cu_2I_2Se_6$ melts congruently at ~ 670 K without superionic transformation.[20] The cyclic Se_6 rings in $Cu_2I_2Se_6$ adopt chair conformation (cyclohexane-like), and the Cu^+ ions have the potential for high ion dynamics, which prompted us to investigate its structural response and electronic properties under high pressure. We observed several drastic and concurrent structural and electronic changes at ~ 21.0 GPa including order-to-disorder transition, the chair-to-planar transformation of Se_6 rings, a collapse of distances along the c-axis, metallization, and emergence of superconductivity. Increasing the pressure within the range of our study up to ~ 41.0 GPa led to a monotonic increase in the onset of the superconducting T_c. DFT calculations reveal an abrupt change in the relative contributions of Se, Cu, and I states to the valence and conduction bands during the metallization and suggest that the drastic conformational changes in the Se_6 rings during metallization lead to a significant contribution from Se states near the Fermi level. We believe the latter critically transforms the electronic band structure of $Cu_2I_2Se_6$ and drives the system to a superconducting state.

■ RESULTS AND DISCUSSION

Structure of Ambient Pressure Phase I. At ambient conditions, $Cu_2I_2Se_6$ crystallizes in the rhombohedral system with space group $R\bar{3}m$ and $Z = 9$ (denoted phase I).[26] This structure consists of infinite neutral cyclic Se_6 rings, which lie parallel to each other in rows stacking along the c axis and are further interconnected through Cu_2I_2 rhomboids to generate a 3D network. Moreover, the structure demonstrates a pillar-layered-like feature, in which the corrugated 2D CuSe layers are interlinked by the Cu_2I_2 rhomboid dimers along the [001] direction (Figures 1a and S1). There are two types of S_3-symmetric cyclic Se_6 rings: ring A (containing three symmetrically equivalent Se2 and three Se3 atoms) and ring B (consisting of six symmetrically equivalent Se1 atoms) (Figure 2a). Both rings adopt chair conformations and resemble the six-membered P_6 rings in black phosphorus. Each ring B is coordinated to six crystallographically equivalent Cu1 atoms

belonging to six Cu_2I_2 rhomboids by Cu1−Se1 bonds (Figure 2a). These rhomboids interact with three Se2 atoms of each neighboring Se_6 ring (A and A′) along the [001] direction. As a consequence, only two-thirds of Se atoms within these three rings are bonded to the Cu atoms (Figure 2a). The Cu1 atoms adopt the tetrahedral sites $18h$ and are coordinated to two iodine atoms (I1) and two Se atoms (Se1 and Se2). These tetrahedra are interconnected in an edge-sharing manner (Figure S2). Under compression, the Cu_2I_2 rhomboids behave as scissor-opening-like distortion, for example, the nearest Cu1−Cu1′ distance is compressed from 3.008(8) to 2.568(4) Å, and the scissor opening angle I1−Cu1−I1′ increases from 110.3(2)° to 119.0(1)° in the range of 0.1 to 12.5 GPa (Figure 2b and Figure S9e). Meanwhile, the Cu1−Se1 and Cu1−Se2 bond lengths are compressed to 2.362(2) and 2.349(3) Å, respectively (Figure S9b).

Structural Phase Transitions under Pressure. We determined the crystal structures of $Cu_2I_2Se_6$ up to 35.8 GPa by synchrotron single crystal X-ray diffraction at room temperature (RT) using helium and 4:1 mixture of methanol−ethanol as the pressure transmitting medium (PTM). From the single crystal X-ray data, we observed two structural phase transitions at ~ 13.0 GPa (I → II) and ~ 21.0 GPa (II → III) (Figures 3 and S3−S5). Despite the pronounced discontinuities of the lattice parameters during these phase transitions, the structure symmetry, $R\bar{3}m$, of $Cu_2I_2Se_6$ is retained in all three phases. The phase I−II transition is characterized by distinct reductions of lattice parameters a and b and an expansion of the c axis under all three different hydrostatic conditions (see Methods). In contrast to the phase I−II transition, the phase II−III transition is accompanied by a striking large collapse of the interlayer distance by $\sim 5.4\%$ (along the c axis) and an unusual negative area expansion of $\sim 3.4\%$ within the ab plane under hydrostatic conditions (with helium used as PTM, see Figure 3a).[27] Interestingly, we find that the high-pressure phase III remains stable to at least 2.9 GPa during decompression (Figures S3−S5). However, the ambient pressure phase I is recovered after the pressure is completely released (Figure S6).

Notably, the main framework of phase I structure is maintained in phase II, and the interstitial site of $6c$ is partially occupied by Cu2 atoms (Figures 1b and 2a). This disorder does not result in any observable diffuse scattering (Figures S4 and S7). The site occupation fraction (SOF) of Cu1 approximately remains constant ($\sim 69.5\%$) throughout phase II region. We find that the Cu2 atoms are encapsulated in a cage comprising three Cu_2I_2 units and two Se_6 rings (A and B). Each Cu2 atom is coordinated by three Se1 atoms (from ring B) and three Se3 atoms (from ring A) with their distances equal to 2.632(3) and 2.577(3) Å, respectively, at 14.4 GPa, which are longer than the sum of Cu and Se covalent radii (2.52 Å).[28] In phase II, the trapped Cu2 atoms hardly change their z-coordinates under pressure (Figure S8) and the "lantern-shaped" unit $[Se_6\text{-Cu-}(Cu_2I_2)_3\text{-}Se_6\text{-Cu-}(Cu_2I_2)_3\text{-}Se_6]$ can be identified as the significant structural variation in comparison to phase I (Figure 2a). Hence, the Cu2−Se1/Se3 distances decrease slightly throughout the phase II region (Figure S9b). In the compressed "lantern-shaped" unit, the Cu_2I_2 rhomboids increase their inclination to the ab plane and a sudden reduction of Cu1−I1 distances is observed (see Figures 1a and S9d). Such a structural deformation leads to a considerable contraction of Cu1−Cu1′ distance, subsequently a strong covalent Cu1−Cu1′ bond is formed, and hence the
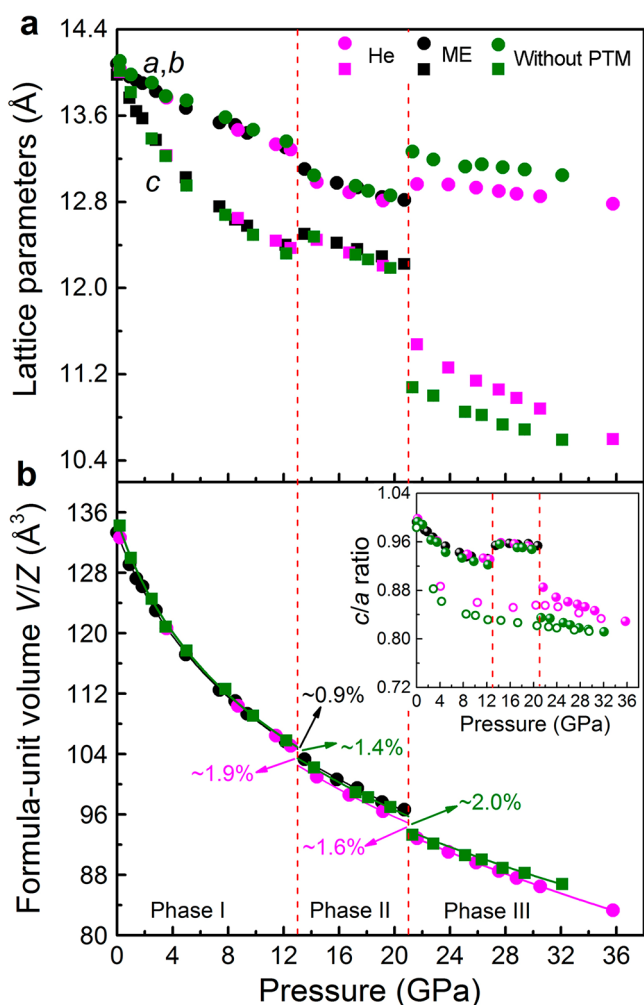
Figure 3. Pressure dependence of lattice parameters in $Cu_2I_2Se_6$ under different hydrostatic conditions. (a) Lattice parameters a, b (circles), and c (squares) as a function of pressure. The magenta and black symbols indicate crystal data collected using helium and methanol−ethanol (ME) mixture as the pressure transmitting medium (PTM), respectively. Moreover, data were also collected without PTM (green symbols) to investigate hydrostaticity on the phase stabilities. (b) The Birch−Murnaghan equation of state (EOS) fits to the formula-unit volume (V/Z) data. These EOS fits have been used for calculating the volume collapses at the transition between phases I/II and II/III. The volume collapses under all three hydrostatic conditions indicate first-order phase transitions. The discrepancy in the volume collapse most likely originates from the different pseudo- and nonhydrostatic pressure environments. The inset enhances the c/a ratio changes as a function of pressure. Unfilled symbols represent decompression data. The calculated bulk moduli are given in Table S1 in the Supporting Information. Vertical red dashed lines indicate phase transition boundaries at approximately 13.0 and 21.0 GPa.

coordination number of Cu1 atom increases from 4 to 5 (Figure S9a). The initial lengths of Cu1−Cu1′ bonds in phase II are comparable to that of phase I at 12.5 GPa (2.57(1) Å), and they gradually reduced to 2.50(2) Å with increasing pressure to 19.2 GPa. The Cu1−Cu1′ bond distances are shorter than that of face-centered-cubic bulk copper (2.56 Å) at ambient pressure.[29]

During the phase II−III transformation, the two disordered Cu atoms remain in the tetrahedral site 18h and interstitial site 6c. However, structural disorder can be directly observed in

pronounced diffuse scattering close to the Bragg peak ($5\bar{1}0$) (Figure S7c). The transformation is accompanied by substantial changes of z-coordinates of Se3 atoms, for example, the z-coordinate decreases from 0.1885(2) at 19.2 GPa (phase II) to 0.1345(13) at 22.0 GPa (phase III), whereas the variations of x- and y-coordinates are negligible (Figure S8). In phase III, the Cu2⋯Se3 lengths increase to 2.955(15) Å, whereas Cu2−Se1 distances suddenly drop to 2.459(12) Å at 22.0 GPa, so that each Cu2 atom is coordinated to only three Se1 atoms. The Cu_2I_2 rhomboids considerably deform with increasing pressure facilitated by the layered-like packing nature of the structure. For example, the scissor opening angle I1−Cu1−I1′ gradually increases to 134.8(7)° at 35.8 GPa (Figure S9e), and the Cu1−Cu1′ bond lengths decrease from 2.50(2) Å (phase II at 19.2 GPa) to 2.13(3) Å at 22.0 GPa (phase III) and gradually to 1.88(3) Å at 35.8 GPa, which are shorter than the Cu−Cu distance of 2.22 Å in an isolated Cu_2 dimer at ambient pressure.[30] The strong anisotropic compression along the c axis drives the Se3 atoms to move progressively closer to the Se2 atoms, reaching comparable z-coordinates at 35.8 GPa (Figure S8). In contrast, the Se1 atoms cannot readily move due to strong Cu1/Cu2−Se1 covalent interactions, and the torsion angles of the Se_6 ring B slightly decrease with increasing pressure (Figure 2c). The substantial conformational changes of Se_6 ring A promote the formation of the new Se2−Se3′ bonds between upper and lower lantern-shaped units, and their distances are substantially reduced (Figures S2 and S9). Subsequently, these units are further linked to each other generating an infinite channel along the c axis (Figure S2). The SOF of the Cu2 atom increases at the expense of Cu1 and reaches 35.7(4)% at 35.8 GPa (Figure 2d). The slow increase of the SOF of the Cu2 atoms above 28.0 GPa implies that their diffusion paths are strongly restricted under compression.

The cyclic Se_6 rings are very sensitive to the external pressure and demonstrate distinct and spectacular conformational changes under compression. To evaluate the distortion of the Se_6 rings under pressure, we analyzed the changes in Se−Se−Se−Se torsion angles (denoted as τ_1 and τ_2 in rings A and B, respectively). In phase I, the Se_6 rings along the c axis interact with Cu_2I_2 rhomboids (Figure 2a). The reduction of the Cu−Se bond lengths and changes of torsion angles τ_1 and τ_2 within rings A and A′ strongly affect the geometrical changes of Cu_2I_2 rhomboids (Figure S9). Obvious discontinuities with a slight increase of τ_1 and reduction of τ_2 are observed in rings A and B during the phase I−II transition. In phase III, the bond lengths and angles of rings A and B vary dramatically. In ring A, the Se2−Se3 length remains virtually constant (~2.11 Å). Meanwhile, the torsion angle τ_1 abruptly decreases by ~71% during the II−III transition and progressively reduces to 7.4(12)° at the experimental limit of 35.8 GPa (Figure 2c). This observation directly confirms that the directional Cu−Se interactions below and above the rings A and A′ are responsible for the substantial decrease in ring strain and the τ_1 angle. These transformations result in a considerable contraction of the Cu1−Se2 bond from 2.26 (2) to 2.13(2) Å, which would enhance the bond interactions (Figure S9). The distinct chair-to-planar conversion of Se_6 rings during the phase II−III transition could be well explained by considerable contraction of the lattice parameter c and interlayer distances. In ring B, during the phase II−III transition and within the phase III range, the torsion angle τ_2 only slightly changes while the Se1−Se1′ bonds hardly compress. The considerable
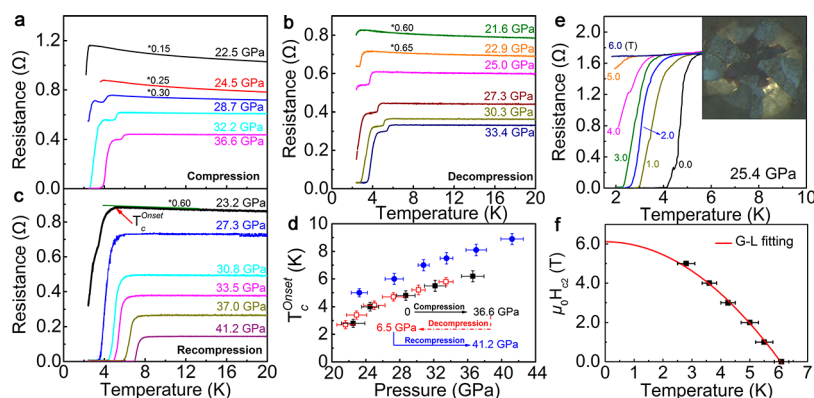
Figure 4. Experimental evidence of pressure-induced superconductivity in $Cu_2I_2Se_6$. (a−c) Temperature-dependent resistance at various pressures in compression, decompression, and recompression cycles in run 2. A step-like transition is observed in compression and decompression cycles; see Supporting Information for more discussion. (d) Evolution of superconducting temperature T_c in compression−decompression-recompression cycles. A prominent enhancement of T_c was observed in the recompression cycle. (e) Temperature-dependent resistances at various magnetic fields from 0.0 to 6.0 T. The inset indicates the photograph of $Cu_2I_2Se_6$ at 25.4 GPa using the four-terminal method for resistivity measurements. (f) Temperature dependence of the superconducting critical field. The curve is fitted with the formula of $H_{c2}(T) = H_{c2}(0)(1 - (T/T_c)^2)/(1 + (T/T_c)^2)$ based on the Ginzburg−Landau (G-L) theory.

anisotropic compression along the c axis in $Cu_2I_2Se_6$ and large distortions of the Cu_2I_2 rhomboids manifest themselves in nearly complete flattening of ring A under further compression, whereas ring B roughly remains undistorted (Figure 2c). This planar Se_6 ring observed in phase III has not been previously observed, either as an isolated molecule or as a ligand in any metal complex.[31−34]

Copper Ion Migrations in Phases II and III. The ionic migration of the small Cu^+ ion (0.6 Å ionic radius) between the interstices in the superionic state have been observed in the matrix compound CuI−VII at 1.3 GPa/966 K.[35−37] Here, we calculated Cu ion diffusion paths and barriers in all three phases of $Cu_2I_2Se_6$ by using the Nudged Elastic Band (NEB) method. We find that the migration from Cu1 site ($18h$) to Cu2 site ($6c$) between two Se_6 rings is an energetically unfavorable path in phase I. However, it is interesting to note that this diffusion pathway is energetically favorable for phase II (Figure S10), and the diffusion barrier is very small, 0.66−0.69 eV. Our results indicate that Cu ions could preferentially diffuse from Cu1 to Cu2 sites in phase II, which may explain the slight increase of SOF of Cu2 atom in this phase regime. In phase III, the migration paths are similar to phase II (Figure S10e). However, the energy barrier of phase III is more than two times higher than that of phase II, which is most likely owing to the restricted free path under high pressure. In the phase III region, the migration barrier increases with pressure as expected from the shortened interatomic distances in the compressed structures.

Pressure-Induced Metallization and Superconductivity. At ambient conditions, $Cu_2I_2Se_6$ has a dark-red appearance and large electrical resistivity ($\sim 10^{12}$ Ω·cm).[20] Under pressure, drastic changes in electronic properties of $Cu_2I_2Se_6$ are observed, which is accompanied by distinct piezochromism (Figure S11). In phase I, the electrical resistance of $Cu_2I_2Se_6$ drops by almost 6 orders of magnitude at RT between 0 and 13.0 GPa. However, the color of the sample remains mostly unchanged, which is consistent with resistance changes as a function of temperature at 10.5 GPa as shown in Figure S12b and DFT calculations (see discussions below). During phase I → II transformation, the crystal color suddenly turns black, and the electrical resistance continues to drop by another order

of magnitude in phase II, while the sample still exhibits semiconducting character (see R−T curves in Figure S12b). In phase III, the sample becomes lustrous and shows good electrical conductivity; however, the electrical resistance slightly increases with decreasing temperature, which is indicative of a poor metal behavior.[38,39] The semiconductor-to-metal transition is consistent with gradual flattening of cyclic rings A in phase III, which drives the corrugated CuSe layer to become conducting. It is notable that the color and resistance changes are irreversible when the sample is quenched to the low pressure of 4.1 GPa, which is consistent with the existence of the quenchable high pressure phase III as discussed before. As soon as the sample entered the phase III region, a sharp drop in electrical resistance at low temperature occurred (e.g., ∼5.5 K at 24.0 GPa in run 1, see Figure S13), which appeared to be the onset of superconducting transition. However, we were unable to see a complete transition because of the experimental limitation on the lower boundary of the temperature. The transition temperature T_c was progressively increased by pressure until we could see a complete transition above ∼30.0 GPa, reaching 8.9 K at the maximum pressure of 41.2 GPa (Figures 4 and 5). Although T_c increases monotonically with increasing pressure in our measured range, an eventual dome-shaped $T_c(P)$ could be expected to develop at even higher pressures.

The presence of bulk superconductivity in $Cu_2I_2Se_6$ was further confirmed with the application of external magnetic field. Figure 4e shows the $T_c(H)$ for $P = 25.4$ GPa. The T_c gradually shifts to lower temperatures with increasing magnetic field, and at 6.0 T, the superconductivity is suppressed below our experimental limit of ∼1.7 K. The upper critical field $\mu_0 H_{c2}$ at 25.4 GPa is determined to be 7.1(1) T according to the Ginzburg−Landau (G-L) formula (Figure 4e). This estimated critical field is much lower than the Bardeen, Cooper, and Schrieffer (BCS) weak-coupling Pauli limiting field $\mu_0 H_p(0) = 1.84 T_c = 11.2$ T.[40]

Electronic Structure. To better understand the electronic evolution of $Cu_2I_2Se_6$ under compression, we performed DFT calculations at selective pressures (Figure 6). The calculated band structures reveal that phase I is an indirect band gap semiconductor with the top of the valence band (VB) located
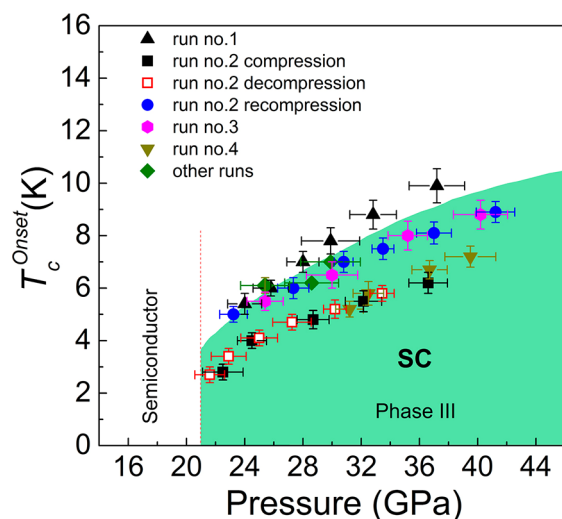
Figure 5. Pressure−temperature phase diagram of $Cu_2I_2Se_6$. The triangles (run 1, compression), squares (run 2 compression), unfilled squares (run 2 decompression), and circles (run 2 recompression) represent the onset of T_c extracted from the electrical resistance measurements. The data from other runs are also plotted. The acronym SC stands for the superconducting state.
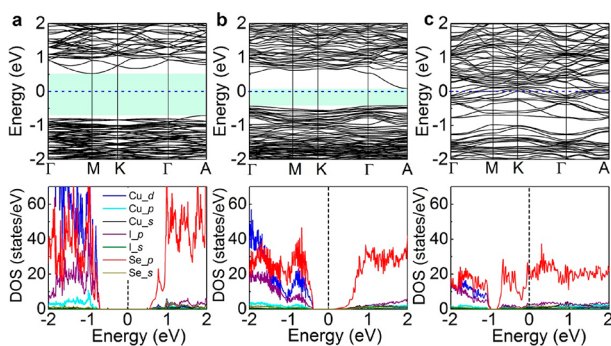

Figure 6. Calculated electronic band structures of $Cu_2I_2Se_6$. Electronic band structures and density of states at (a) 0.2 GPa (phase I), (b) 14.4 GPa (phase II), and (c) 22.0 GPa (phase III). The Fermi level is set to zero energy, shown by the dashed line in each plot.

at "A" k-point (0.0 0.0 0.5) and the bottom of the conduction band (CB) located at "M" k-point (0.0 0.5 0.0). It is interesting to note that an indirect (A−M) to direct (A−A) electronic band gap transition is observed in phase I at 12.5 GPa (Figure S14). The competition between M (in-plane k-point) and A (locals at out of xy-plane) of the conduction band minimum (CBM) determines whether phase I is a direct or indirect semiconductor. We do not observe an apparent change of the band gap in phase I, which agrees well with the experimental observation of slight color change in phase I (Figures S11 and S15). During the phase I−II transition, the band gap is drastically reduced, from 1.19 eV at 12.5 GPa to 0.51 eV at 14.4 GPa, which indicates that the compound is still a semiconductor. The metallic band structure is observed in the phase III regime, which is in good agreement with the electrical transport measurements. To investigate the nature of CBM, especially M and A k-points, the band decomposed charge density plots are displayed in Figure S16. In phase I, M k-point is mainly comprised of Se-4p states that align head-to-head in the Se_6 ring. Such orientation does not change with increasing

pressure. However, the orientations of Se-4p orbitals of A k-point changed from head-to-tail (0.2 GPa) to center-focus (8.7 and 12.5 GPa). Obviously, the center-focus type orientation certainly enhances the bonding character of Se-4p states, that is, an energy red shift of A k-point at 8.7 and 12.5 GPa compared to that of A k-point at 0.2 and 3.5 GPa. Therefore, the competition between M and A in phase I are most likely because of the pressure-induced orientation transition of Se-4p orbitals. In contrast to phase I, the M k-point in phase II can be easily distinguished, since the Se atoms within the Se_6 rings demonstrate strong antibonding character. For the A k-point, the orientations of Se-4p states in phase II are similar to that of phase I at 12.5 GPa, but they exhibit strong bonding character with newly emerged Cu2 ions. Because of these enhanced bonding states, the energy of A k-point in phase II is much lower than that in phase I at 12.5 GPa. This could explain the drastic reduction of band gap during the phase I−II transition.

In order to understand the contributions of Cu, I, and Se orbital states in the three phases, we plot the density of states (DOS) as a function of pressure (Figures 6 and S17). Here, we compare the DOS in three selected pressure points of 0.2, 14.4, and 22.0 GPa for phases I, II, and III, respectively (Figure 6). In phase I (0.2 GPa), the valence bands are mainly occupied by Se-4p states with several Cu-4s and I-5p states, while Se-4p states dominate the conduction bands. A similar situation is found in phase II (14.4 GPa). In contrast, in phase III (22.0 GPa), Se states make the most contribution to the bands around the Fermi level. The significant contribution of Se states around the Fermi level indicates that the Se_6 rings are critical to the electronic band structures and reflect the considerable conformational changes of these Se_6 rings in phase III (Figure S17). Therefore, the flattened Se_6 rings are responsible for a high density of states at the Fermi level, which is connected with the occurrence of superconductivity in phase III. Moreover, we can see that the calculated DOS near the Fermi level further increases with pressure, which is correlated with the enhancement of the superconducting temperature T_c (Figure S18). Furthermore, the localization of I-5p and Se-4p lone pair states and the origin of metallization in phase III have been investigated by electron localization function (ELF, see Figure S19).[41] In phases I and II, the Se-4p states aligned with the I-5p lone pair states, while lone pair states of Se-4p and I-5p break off in phase III, and some kind of delocalized bonding states are formed predominately around Se_6 rings. Therefore, phase III is a poor metal, which is mainly due to the metallic states tightly surrounding Se_6 layers.

The signature of diamagnetism in ambient pressure phase I reveals the copper ion should be monovalent (+1) (Figure S20). One interesting possibility to consider is the change of Cu oxidation level under pressure due to formation of new Cu−Cu bonds. We closely examined this scenario; however, our DFT calculations do not suggest any considerable change in the magnetic moment of Cu in any of the three phases. Furthermore, the Bader charge[42,43] of Cu atoms does not show any considerable change throughout the measured pressure range, for example, 0.30 e (at 0.2 GPa, phase I) vs 0.33 e (at 31.6 GPa, phase III) (see Figure S21). The increase of valence state generally accompanies large charge change.[44] Hence, this analysis suggests that +1 oxidation state in Cu atom should be maintained in all three phases. Therefore, we do not find evidence of change in the valence state of the Cu atoms under pressure or during the phase transitions.

CONCLUSIONS

The high pressure phase III of $Cu_2I_2Se_6$ eliminates the wide band gap of 1.95 eV and represents a surprising new example of Cu-containing superconductor that remains metastable to ~3.0 GPa during decompression. Electrical transport measurements and DFT calculations reveal the semiconductor-to-metal transition and the emergence of superconductivity. Further chemical modification (e.g., tellurium substitution) could shift the superconducting transition pressure to a lower accessible range and may allow recovering the metastable superconducting phase at ambient pressure. The unanticipated planar Se_6 ring, an unknown modification up to this point, is observed in this material while the initial crystal symmetry is maintained during two unique order-to-disorder phase transitions. Flat Se_6 rings are unknown at ambient conditions because energetically they lie much above the chair-conformation ground state. Therefore, the pressure imposed flattening of the rings significantly elevates the energies of the HOMO levels and brings them well into the band gap to cause metallization of the overall system. The flattening of the rings however does not amount to aromatization because the latter implies stabilization and energy gap creation (e.g., a HOMO–LUMO gap in aromatic molecules). We also find the tetrahedrally coordinated Cu atoms partially migrate to interstitial sites and are encapsulated in cages comprised of Cu_2I_2-rhomboids and cyclic Se_6 rings in phase II and III. The cyclohexane-like conformation of the Se_6 rings with their S_3-symmetry axis parallel to the c axis imparts the rhombohedral structure of the $Cu_2I_2Se_6$ a particularly soft direction. The flattening of these rings with moderate pressure is responsible for the complete closing of such a wide energy band gap to yield a metal and a superconductor.

In high-T_c cuprates, the superconductivity occurs in the CuO_2 square lattice, where the Cu^{2+} ions are antiferromagnetically ordered. After appropriate elemental (hole or electron) doping, the AFM order is suppressed, which is followed by the emergence of superconductivity. Similar square-lattice geometry was also observed in corrugated FeSe-layer of FeSCs. The high-pressure phase III of $Cu_2I_2Se_6$ represents a unique rhombohedral superconducting structure in which the parent compound does not exhibit magnetic order (Figure S22). This observation of superconductivity in a novel lattice type comprised of nonmagnetic copper ions in $Cu_2I_2Se_6$ provides a route to seek new copper-containing superconductors in other analogous families of materials.

EXPERIMENTAL METHODS

Sample Synthesis. High purity dark-red single crystals of $Cu_2I_2Se_6$ were synthesized as described previously.[20] The specific synthesis procedures are described in the Supporting Information. The crystals are well characterized by means of powder X-ray diffraction.

High-Pressure X-ray Diffraction Measurements. The Boehler–Almax plate diamond anvil cells (DACs) with large opening angle (500 μm culet size) were used for all X-ray diffraction measurements at RT. The pressure was calibrated by the ruby fluorescence method.[45] In order to reduce the uncertainty of pressure, the pressure was measured before and after each diffraction data collection. To ensure a good hydrostatic environment and compare quasi-hydrostatic stress on the phase stabilities of $Cu_2I_2Se_6$, methanol–ethanol (ME, volume ratio 4:1) and helium were used as pressure-transmitting media (PTM). Single crystals of $Cu_2I_2Se_6$ were loaded in ~180 μm diameter stainless steel gasket chambers. All high-pressure single crystal X-ray diffraction measurements were conducted at beamline 13-BM-C, GSECARS of the Advanced Photon Source (APS), Argonne National Laboratory (ANL) (λ = 0.4325 Å). The ATREX/RSV IDL software package was used to perform the diffraction data reduction.[46] The crystal structures of $Cu_2I_2Se_6$ were solved by direct methods with the aid of SHELXL-97.[47] In order to mimic similar conditions to those for electric resistance measurements, the powder X-ray diffraction data of $Cu_2I_2Se_6$ polycrystalline samples without PTM were collected at 16-ID-B beamline of the High Pressure Collaborative Access Team (HPCAT) at APS, ANL (λ = 0.4066 Å). The image data were integrated using the *Dioptas* program.[48] The X-ray diffraction data were analyzed by Le Bail fitting method using GSAS-EXPGUI package.[49] All the refinement details are provided in the Supporting Information (see Tables S2–S4).

High Pressure Electrical Transport Measurements. Electric resistance measurements of $Cu_2I_2Se_6$ powder were performed by the quasi-four- and four-terminal method without PTM. Fine alumina and epoxy mixture was used as an insulation layer. Platinum leads were arranged to measure the resistance of the sample by the quasi-four- and four-terminal technique. A Stanford Research SR830 digital lock-in amplifier was used for temperature-dependent resistance measurements in a closed cycle He cryostat (2.4–300 K). Data on electrical resistances at various magnetic fields were collected in a Janis SuperOptiMag liquid helium cryostat system (1.7–300 K, 0–7 T) using a nonmagnetic copper beryllium (CuBe) DAC. The pressure was measured at both RT and low temperature in all runs.

DFT Calculations. Electronic structure calculations were performed using the Vienna ab initio simulation package (VASP)[50] in the framework of density functional theory (DFT). The general gradient approximation (GGA) functional of Perdew–Burke–Ernzerhof (PBE)[51] was employed. The plane wave basis with the frozen-core projector augmented wave (PAW) potential[52,53] and a plane wave cut off energy of 400 eV were used. We used the nudged elastic band (NEB) method[54] to evaluate the barrier of Cu diffusion from site 18h to site 6c. The NEB calculations were performed with 7–11 relaxed images. For the electronic structure calculations, a 3 × 3 × 3 Monkhorst–Pack k mesh was used in the self-consistent field (SCF) ground state calculations. Then a dense k grid of 9 × 9 × 9 was employed in the calculation of density of states. Because of the fractional occupation of Cu in phases II and III, the conventional cell (hexagonal cell) was used and Cu positions were selected randomly. Therefore, the k-path in band structure is changed from Γ-P-Z-Q-Γ-F-P1-Q1-L-Z (rhombohedral) to Γ-M-K-Γ-A (hexagonal), as shown in Figure S23.

ASSOCIATED CONTENT

Ⓢ Supporting Information

The Supporting Information is available free of charge on the ACS Publications website at DOI: 10.1021/jacs.9b06794.

Detailed experimental procedures, supplementary discussions, Figures S1–S23, and Tables S1–S4 (PDF)

X-ray crystallographic data in CIF format for three phases of $Cu_2I_2Se_6$ (CIF)

AUTHOR INFORMATION

Corresponding Authors

*longhuali@ujs.edu.cn
*m-kanatzidis@northwestern.edu
*Deemyad@physics.utah.edu

ORCID Ⓞ

Weizhao Cai: 0000-0001-7805-2108
Long-Hua Li: 0000-0003-1817-5039
Christos D. Malliakas: 0000-0003-4416-638X
Jin-Ke Bao: 0000-0001-5522-3605
Dongzhou Zhang: 0000-0002-6679-892X
Mercouri G. Kanatzidis: 0000-0003-2037-4168
Shanti Deemyad: 0000-0001-5661-8801

■ REFERENCES

(1) Bednorz, J. G.; Müller, K. A. Possible high Tc superconductivity in the Ba−La−Cu−O system. *Z. Phys. B: Condens. Matter* **1986**, *64*, 189−193.

(2) Cava, R. J.; Batlogg, B.; van Dover, R. B.; Murphy, D. W.; Sunshine, S.; Siegrist, T.; Remeika, J. P.; Rietman, E. A.; Zahurak, S.; Espinosa, G. P. Bulk superconductivity at 91 K in single-phase oxygen-deficient perovskite $Ba_2YCu_3O_{9-\delta}$. *Phys. Rev. Lett.* **1987**, *58*, 1676−1679.

(3) Hor, P. H.; Gao, L.; Meng, R. L.; Huang, Z. J.; Wang, Y. Q.; Forster, K.; Vassilious, J.; Chu, C. W.; Wu, M. K.; Ashburn, J. R.; Torng, C. J. High-pressure study of the new Y-Ba-Cu-O superconducting compound system. *Phys. Rev. Lett.* **1987**, *58*, 911−912.

(4) Schilling, A.; Cantoni, M.; Guo, J. D.; Ott, H. R. Superconductivity above 130 K in the Hg−Ba−Ca−Cu−O system. *Nature* **1993**, *363*, 56.

(5) Bednorz, J. G.; Muller, K. A. Perovskite-type oxides—The new approach to high-T_c superconductivity. *Rev. Mod. Phys.* **1988**, *60*, 585−600.

(6) Kancharla, S. S.; Kyung, B.; Sénéchal, D.; Civelli, M.; Capone, M.; Kotliar, G.; Tremblay, A. M. S. Anomalous superconductivity and its competition with antiferromagnetism in doped Mott insulators. *Phys. Rev. B: Condens. Matter Mater. Phys.* **2008**, *77*, 184516.

(7) Nagaosa, N. Superconductivity and Antiferromagnetism in High-T_c Cuprates. *Science* **1997**, *275*, 1078.

(8) Kloss, T.; Montiel, X.; de Carvalho, V. S.; Freire, H.; Pépin, C. Charge orders, magnetism and pairings in the cuprate superconductors. *Rep. Prog. Phys.* **2016**, *79*, 084507.

(9) Kamihara, Y.; Watanabe, T.; Hirano, M.; Hosono, H. Iron-Based Layered Superconductor $La[O_{1-x}F_x]FeAs$ (x = 0.05−0.12) with T_c = 26 K. *J. Am. Chem. Soc.* **2008**, *130*, 3296−3297.

(10) Guo, J.; Jin, S.; Wang, G.; Wang, S.; Zhu, K.; Zhou, T.; He, M.; Chen, X. Superconductivity in the iron selenide $K_xFe_2Se_2$ ($0 \leq x \leq$ 1.0). *Phys. Rev. B: Condens. Matter Mater. Phys.* **2010**, *82*, 180520.

(11) Hsu, F.-C.; Luo, J.-Y.; Yeh, K.-W.; Chen, T.-K.; Huang, T.-W.; Wu, P. M.; Lee, Y.-C.; Huang, Y.-L.; Chu, Y.-Y.; Yan, D.-C.; Wu, M.-K. Superconductivity in the PbO-type structure α-FeSe. *Proc. Natl. Acad. Sci. U. S. A.* **2008**, *105*, 14262−14264.

(12) Paglione, J.; Greene, R. L. High-temperature superconductivity in iron-based materials. *Nat. Phys.* **2010**, *6*, 645.

(13) Han, F.; Zhu, X.; Cheng, P.; Mu, G.; Jia, Y.; Fang, L.; Wang, Y.; Luo, H.; Zeng, B.; Shen, B.; Shan, L.; Ren, C.; Wen, H.-H. Superconductivity and phase diagrams of the 4d and 5d-doped iron arsenides $SrFe_{2-x}M_xAs_2$ (M = Rh, Ir, Pd). *Phys. Rev. B: Condens. Matter Mater. Phys.* **2009**, *80*, 024506.

(14) Chu, C. W.; Gao, L.; Chen, F.; Huang, Z. J.; Meng, R. L.; Xue, Y. Y. Superconductivity above 150 K in $HgBa_2Ca_2Cu_3O_{8+\delta}$ at high pressures. *Nature* **1993**, *365*, 323.

(15) Sun, L.; Chen, X.-J.; Guo, J.; Gao, P.; Huang, Q.-Z.; Wang, H.; Fang, M.; Chen, X.; Chen, G.; Wu, Q.; Zhang, C.; Gu, D.; Dong, X.; Wang, L.; Yang, K.; Li, A.; Dai, X.; Mao, H.-k.; Zhao, Z. Re-emerging superconductivity at 48 K in iron chalcogenides. *Nature* **2012**, *483*, 67.

(16) Medvedev, S.; McQueen, T. M.; Troyan, I. A.; Palasyuk, T.; Eremets, M. I.; Cava, R. J.; Naghavi, S.; Casper, F.; Ksenofontov, V.; Wortmann, G.; Felser, C. Electronic and magnetic phase diagram of β-$Fe_{1.01}$Se with superconductivity at 36.7 K under pressure. *Nat. Mater.* **2009**, *8*, 630.

(17) Takahashi, H.; Sugimoto, A.; Nambu, Y.; Yamauchi, T.; Hirata, Y.; Kawakami, T.; Avdeev, M.; Matsubayashi, K.; Du, F.; Kawashima, C.; Soeda, H.; Nakano, S.; Uwatoko, Y.; Ueda, Y.; Sato, T. J.; Ohgushi, K. Pressure-induced superconductivity in the iron-based ladder material $BaFe_2S_3$. *Nat. Mater.* **2015**, *14*, 1008.

(18) Uehara, M.; Nagata, T.; Akimitsu, J.; Takahashi, H.; Môri, N.; Kinoshita, K. Superconductivity in the Ladder Material $Sr_{0.4}Ca_{13.6}Cu_{24}O_{41.84}$. *J. Phys. Soc. Jpn.* **1996**, *65*, 2764−2767.

(19) Wang, Y.; Ying, J.; Zhou, Z.; Sun, J.; Wen, T.; Zhou, Y.; Li, N.; Zhang, Q.; Han, F.; Xiao, Y.; Chow, P.; Yang, W.; Struzhkin, V. V.; Zhao, Y.; Mao, H.-k. Emergent superconductivity in an iron-based honeycomb lattice initiated by pressure-driven spin-crossover. *Nat. Commun.* **2018**, *9*, 1914.

(20) Lin, W.; Stoumpos, C. C.; Kontsevoi, O. Y.; Liu, Z.; He, Y.; Das, S.; Xu, Y.; McCall, K. M.; Wessels, B. W.; Kanatzidis, M. G. $Cu_2I_2Se_6$: A Metal-inorganic Framework Wide-Bandgap Semiconductor for Photon Detection at Room Temperature. *J. Am. Chem. Soc.* **2018**, *140*, 1894−1899.

(21) Hull, G. W.; Hulliger, F. $CuSe_2$, a Marcasite Type Superconductor. *Nature* **1968**, *220*, 257−258.

(22) Gonçalves, A. P.; Lopes, E. B.; Casaca, A.; Dias, M.; Almeida, M. Growth of CuS platelet single crystals by the high-temperature solution growth technique. *J. Cryst. Growth* **2008**, *310*, 2742−2745.

(23) Hull, S. Superionics: crystal structures and conduction processes. *Rep. Prog. Phys.* **2004**, *67*, 1233−1314.

(24) Keen, D. A. Disordering phenomena in superionic conductors. *J. Phys.: Condens. Matter* **2002**, *14*, R819.

(25) Deiseroth, H.-J.; Reiner, C.; Schlosser, M.; Wang, X.; Ajaz, H.; Kienle, L. Cyclic Se_6 and Helical $[Se_x]$ as Neutral Ligands in the New Compounds $PdBr_2Se_6$ and $PdCl_2Se_8$. *Inorg. Chem.* **2007**, *46*, 8418−8425.

(26) Milius, W.; Rabenau, A. The crystal structure of copper iodide triselenide $CuISe_3$, a reactant in an n-$CuInSe_2$ based solar cell. *Mater. Res. Bull.* **1987**, *22*, 1493−1497.

(27) Zieliński, W.; Katrusiak, A. Colossal Monotonic Response to Hydrostatic Pressure in Molecular Crystal Induced by a Chemical Modification. *Cryst. Growth Des.* **2014**, *14*, 4247−4253.

(28) Cordero, B.; Gómez, V.; Platero-Prats, A. E.; Revés, M.; Echeverría, J.; Cremades, E.; Barragán, F.; Alvarez, S. Covalent radii revisited. *Dalton Trans.* **2008**, 2832−2838.

(29) Donohue, J. *The Structures of the Elements*; Wiley: New York, 1974.

(30) Jaque, P.; Toro-Labbé, A. Characterization of copper clusters through the use of density functional theory reactivity descriptors. *J. Chem. Phys.* **2002**, *117*, 3208−3218.

(31) Miyamoto, Y. Structure and Phase Transformation of Rhombohedral Selenium Composed of Se_6 Molecules. *Jpn. J. Appl. Phys.* **1980**, *19*, 1813.

(32) Dickerson, C. A.; Fisher, M. J.; Sykora, R. E.; Albrecht-Schmitt, T. E.; Cody, J. A. Solvothermal Synthesis and Structure of a New Selenium-Rich Selenophosphate $K_3PSe_4·2Se_6$. *Inorg. Chem.* **2002**, *41*, 640−642.

(33) Aris, D.; Beck, J.; Decken, A.; Dionne, I.; Krossing, I.; Passmore, J.; Rivard, E.; Steden, F.; Wang, X. The Metastable Partially Positively Charged Se_6 Molecule: Preparation, Characterisation and X-ray Crystal Structure of $[Ag_2(Se_6)(SO_2)_2][Sb(OTeF_5)_6]_2$, $[Ag_2Se_6][AsF_6]_2$ and $[AgSe_6][Ag_2(SbF_6)_3]$. *Phosphorus, Sulfur Silicon Relat. Elem.* **2004**, *179*, 859−863.

(34) Aris, D.; Beck, J.; Decken, A.; Dionne, I.; Schmedt auf der Gunne, J.; Hoffbauer, W.; Kochner, T.; Krossing, I.; Passmore, J.; Rivard, E.; Steden, F.; Wang, X. Metastable Se_6 as a ligand for Ag^+: from isolated molecular to polymeric 1D and 2D structures. *Dalton Trans.* **2011**, *40*, 5865−5880.

(35) Hull, S.; Keen, D. A.; Hayes, W.; Gardner, N. J. G. Superionic behaviour in copper (I) iodide at elevated pressures and temperatures. *J. Phys.: Condens. Matter* **1998**, *10*, 10941.

(36) Hofmann, M.; Hull, S.; Keen, D. A. High-pressure phase of copper(I) iodide. *Phys. Rev. B: Condens. Matter Mater. Phys.* **1995**, *51*, 12022−12025.

(37) Keen, D. A.; Hull, S. The high-temperature structural behaviour of copper(I) iodide. *J. Phys.: Condens. Matter* **1995**, *7*, 5793.

(38) Emery, V. J.; Kivelson, S. A. Superconductivity in Bad Metals. *Phys. Rev. Lett.* **1995**, *74*, 3253−3256.

(39) Fang, M.-H.; Wang, H.-D.; Dong, C.-H.; Li, Z.-J.; Feng, C.-M.; Chen, J.; Yuan, H. Q. Fe-based superconductivity with T_c = 31 K bordering an antiferromagnetic insulator in (Tl,K) Fe_xSe_2. *Europhys. Lett.* **2011**, *94*, 27009.

(40) Clogston, A. M. Upper Limit for the Critical Field in Hard Superconductors. *Phys. Rev. Lett.* **1962**, *9*, 266−267.

(41) Savin, A.; Nesper, R.; Wengert, S.; Fässler, T. F. ELF: The Electron Localization Function. *Angew. Chem., Int. Ed. Engl.* **1997**, *36*, 1808−1832.

(42) Bader, R. *Atoms in Molecules: A Quantum Theory*; Oxford University Press: 1990.

(43) Henkelman, G.; Arnaldsson, A.; Jónsson, H. A fast and robust algorithm for Bader decomposition of charge density. *Comput. Mater. Sci.* **2006**, *36*, 354−360.

(44) Miao, M.-s. Caesium in high oxidation states and as a p-block element. *Nat. Chem.* **2013**, *5*, 846.

(45) Mao, H. K.; Bell, P. M.; Shaner, J. W.; Steinberg, D. J. Specific volume measurements of Cu, Mo, Pd, and Ag and calibration of the ruby R_1 fluorescence pressure gauge from 0.06 to 1 Mbar. *J. Appl. Phys.* **1978**, *49*, 3276−3283.

(46) Dera, P.; Zhuravlev, K.; Prakapenka, V.; Rivers, M. L.; Finkelstein, G. J.; Grubor-Urosevic, O.; Tschauner, O.; Clark, S. M.; Downs, R. T. High pressure single-crystal micro X-ray diffraction analysis with GSE_ADA/RSV software. *High Pressure Res.* **2013**, *33*, 466−484.

(47) Sheldrick, G. A short history of SHELX. *Acta Crystallogr., Sect. A: Found. Crystallogr.* **2008**, *64*, 112−122.

(48) Prescher, C.; Prakapenka, V. B. DIOPTAS: a program for reduction of two-dimensional X-ray diffraction data and data exploration. *High Pressure Res.* **2015**, *35*, 223−230.

(49) Toby, B. EXPGUI, a graphical user interface for GSAS. *J. Appl. Crystallogr.* **2001**, *34*, 210−213.

(50) Kresse, G.; Furthmüller, J. Efficient iterative schemes for ab initio total-energy calculations using a plane-wave basis set. *Phys. Rev. B: Condens. Matter Mater. Phys.* **1996**, *54*, 11169−11186.

(51) Perdew, J. P.; Burke, K.; Ernzerhof, M. Generalized Gradient Approximation Made Simple. *Phys. Rev. Lett.* **1996**, *77*, 3865−3868.

(52) Blöchl, P. E. Projector augmented-wave method. *Phys. Rev. B: Condens. Matter Mater. Phys.* **1994**, *50*, 17953−17979.

(53) Kresse, G.; Joubert, D. From ultrasoft pseudopotentials to the projector augmented-wave method. *Phys. Rev. B: Condens. Matter Mater. Phys.* **1999**, *59*, 1758−1775.

(54) Henkelman, G.; Uberuaga, B. P.; Jónsson, H. A climbing image nudged elastic band method for finding saddle points and minimum energy paths. *J. Chem. Phys.* **2000**, *113*, 9901−9904.